Radiation Energy and Mutual Coupling Evaluation for Multimode MIMO Antenna Based on the Theory of Characteristic Mode

Wei Su, Qianyun Zhang, *Member, IEEE*, Shaker Alkaraki, *Student Member, IEEE*, Yao Zhang, Xiu-Yin Zhang, *Senior Member, IEEE*, and Yue Gao, *Senior Member, IEEE*

***Abstract*— This paper presents a novel method to evaluate radiation energy and mutual coupling in multimode antennas. Based on the theory of characteristics mode, how much each mode occupies the radiation and the mutual coupling from each feeding port is calculated with the modal energy occupied coefficients. Furthermore, the linear transformation of feeding network in multimode antenna system has been adopted to complete the modal-based method. Then, this method is utilized to analyze and decrease the mutual coupling between feeding ports. Hence, a hexagonal wideband antenna is proposed with its evolution process and measured to validate the proposed method. The presented hexagonal antenna is a four-port multimode antenna consisting a planar hexagonal plate, vertical tapered baluns, and feeding network at the ground plane. The whole antenna works in 3–6 GHz and all its four ports are well matched with high port-to-port isolation.**

***Index Terms*— Characteristic mode (CM), multimode antenna, multiple-input multiple-output (MIMO) antenna, mutual coupling.**

I. Introduction

RESEARCH and development on the design of multimode antennas have attracted considerable attention in recent years. Radiating multiple modes through different excitations on one structure [1]–[5], the multimode antenna could avoid the large spatial requirement of a conventional multiple-input multiple-output (MIMO) array and can be a competitive candidate in the construction of massive MIMO systems [6]. The idea of using the theory of characteristic mode (TCM) to design multimode antennas by directly placing feedings on antennas has been introduced in [7] and [8], and since then, multiport antenna design has become one of the important applications of TCM.

Manuscript received March 27, 2018; revised September 11, 2018; accepted October 5, 2018. Date of publication November 1, 2018; date of current version January 16, 2019. This work was supported in part by the Macau Polytechnic Institute and in part by the National Natural Science Foundation of China under Grant 61828102. *(Corresponding author: Qianyun Zhang.)*

W. Su, Q. Zhang, S. Alkaraki, and Y. Gao are with the School of Electronic Engineering and Computer Science, Queen Mary University of London, London E1 4NS, U.K. (e-mail: w.su@qmul.ac.uk; qianyun.zhang@qmul.ac.uk; s.m.alkaraki@qmul.ac.uk; yue.gao@qmul.ac.uk).

Y. Zhang and X.-Y. Zhang are with the School of Electronic and Information Engineering, South China University of Technology, Guangzhou 510641, China (e-mail: zhangsantu123@sina.cn; zhangxiuyin@scut.edu.cn).

Color versions of one or more of the figures in this paper are available online at http://ieeexplore.ieee.org.

Digital Object Identifier 10.1109/TAP.2018.2878078

Providing distinct insights into operating mechanisms of antennas, TCM significantly benefits the design of multimode antennas [6]–[11]. As modal far-field patterns are orthogonal to each other, exciting pure characteristic modes (CMs) through specific feeding methods leads to high port-to-port isolations. In [11], a four-mode MIMO antenna covering a tunable frequency from 470 to 790 MHz was realized on a femto-cell factor structure. A $220 \times 220 \times 140$ mm^3 box was analyzed with TCM, and the four modes were excited through an internal tunable matching network. By inserting symmetry slots on a square plate, Manteuffel and Martens [6] excited four CMs simultaneously on the plate to achieve a compact multimode antenna element with four ports. Afterward, the optimized four-port antenna element was extended to an 11×11 array with 484 ports for massive MIMO applications.

The design of multimode antennas is challenging since all ports have to be well matched while maintaining high port-to-port isolations at the same time. Although the TCM has been proven to be a useful tool to tackle some of the challenges in the design of multimode antennas [6]–[11], it also reaches the limit.

First, the requirement for multiple input ports means that CM analysis (CMA) should focus on more than two potential CMs, which implies that the maximum dimension of the antenna is larger than half of the operating wavelength, instead of being electrically small [12]. In this case, some low-order CMs have already passed their resonant frequency but still have potentials to radiate, while others are approaching their resonance. Thence, it is difficult to solely excite a pure CM from each feeding port. Previous multiport antennas realized with TCM [6]–[10], only considered the resonating CMs, while the near-resonating CMs and nonresonating ones were ignored. This made the outcome antenna performance more or less different from the performance of the single CM. In addition, most CMA-related literature [6]–[8] developed their feeding ports just from feeding positions suggested by CMA (i.e., the current maxima of the corresponding mode to be excited). However, these are not always easy to discern and locate on the antenna structure due to the complexity of high-order CMs current distributions. Moreover, in most cases, feeding positions are not only just decided according to the CMA results but also the requirement of easy-to-fabricate

or esthetic needs. In general, excitations of CMs will not always be as ideal as designers' expectations and they may deteriorate the final antenna performance. Therefore, a CMA-based method with respect to predetermined input ports helps to overcome these problems.

In [13], CMA has been used to reduce the out-of-band coupling, as the evaluation of mutual coupling was introduced as a modal admittance (MA). Moreover, it showed that the modal mutual coupling is able to be calculated between CMs and it can be used to identify certain CMs to suppress. However, the proposed work in [13] only discussed a two-element system and did not address the design of multimode MIMO antennas.

In this paper, a new method to evaluate the CM radiation and coupling is presented. Supported with theoretical analyses and derivations, the proposed method is enabled to be adopted to analyze multimode antenna systems. Based on the method, a four-port wideband antenna with its evolution process is given as an example. The antenna works from 3 to 6 GHz, and it realizes a high isolation among each port. All CMA in this paper are calculated under MATLAB environment with impedance matrix generated from FEKO, and the final antenna design is optimized in CST Microwave Studio.

II. Mutual Coupling in the CMA Sense

First, presented by Garbacz and Turpin [14], the TCM was then refined and analyzed with comprehensive depiction by Harrington and Mautz [15] and Harrington *et al.* [16] with linear operators. For any conducting body with incident electromagnetic wave on its surface, the surface current $\mathbf{J}$ and scattering field $\mathbf{E}$ can be decomposed into several CMs

$$\mathbf{J} = \sum_{n=1}^{\infty} \frac{V_n^i \mathbf{J}_n}{1 + j\lambda_n} = \sum_{n=1}^{\infty} \frac{\langle \mathbf{J}_n, \mathbf{E}^i \rangle}{1 + j\lambda_n} \mathbf{J}_n \tag{1}$$

$$\mathbf{E} = \sum_{n=1}^{\infty} \frac{V_n^i \mathbf{E}_n}{1 + j\lambda_n} = \sum_{n=1}^{\infty} \frac{\langle \mathbf{J}_n, \mathbf{E}^i \rangle}{1 + j\lambda_n} \mathbf{E}_n \tag{2}$$

where λ_n, $\mathbf{J}_n$, and $\mathbf{E}_n$ are eigenvalue, modal current, and modal field for the n_{th} mode, respectively. V_n^i denotes the modal excitation coefficient, which is the inner product of two vectors: $\mathbf{J}_n$ and incident excitation $\mathbf{E}^i$. It is worth mentioning that the eigenvalue, one of the most simple yet crucial properties of a CM, plays an important role as indicating the radiating ability of each mode. For arbitrary Mode m and n, there is [15]

$$\lambda_n \delta_{mn} = \omega \iint_S \left(\mu H_m \cdot H_n^* - \epsilon E_m \cdot E_n^* \right) d\Omega \tag{3}$$

where μ and ϵ are the permittivity and permeability of free space, respectively, and δ_{mn} is the Kronecker delta

$$\delta_{mn} = \begin{cases} 1, & m = n \\ 0, & m \neq n. \end{cases}$$

According to (3), when $m = n$, the sign of eigenvalue λ_n determines the kind of energy this mode stores: when $\lambda_n > 0$, Mode n stores magnetic energy, while when $\lambda_n < 0$, Mode n stores electric energy. Equation (3) also indicates that the smaller λ_n is, the more energy its corresponding mode could radiate. The radiation ability of one mode can be indicated by the modal significance (MS) [17], which is defined as

$$MS = \left| \frac{1}{1 + j\lambda} \right|. \tag{4}$$

MS is always smaller than 1. The closer it is to 1, the more likely the mode resonates. CMs with $MS < 1/\sqrt{2}$ are referred to as "nonsignificant modes" [17] that are normally ignored in CMA.

When a unit incident excitation occurs at the p_{th} mesh edge, it can be expressed as [13], [18]

$$\mathbf{E}^i = \mathbf{e}_p \delta(\mathbf{r}') \tag{5}$$

where $\mathbf{e}_p$ is a unit vector normal to the p_{th} edge and $\mathbf{r}'$ is a radius vector. The modal excitation coefficient V_n^i is obtained from [13]

$$V_n^i = V_1 I_n(p) l_p \tag{6}$$

where V_1 is the magnitude of the input excitation. $I_n(p)$ is the p_{th} current coefficient for the n_{th} modal current and l_p is the corresponding edge length.

Furthermore, the radiation power P_{rad} of the output wave at infinite writes

$$P_{rad} = \frac{1}{\eta} \iint_{S_\infty} \mathbf{E} \cdot \mathbf{E}^* d\Omega. \tag{7}$$

Apply simplified modal coefficients given by (6), the decomposition of E-field in (2) and their orthogonality [17]

$$\frac{1}{\eta} \iint_{S_\infty} \mathbf{E_m} \cdot \mathbf{E_n}^* d\Omega = \delta_{mn} \tag{8}$$

to (7) and get

$$\begin{aligned} P_{rad} &= \frac{1}{\eta} \iint_{S_\infty} \sum_{n=1}^{\infty} \frac{V_n^i \mathbf{E}_n}{1 + j\lambda_n} \cdot \left(\sum_{m=1}^{\infty} \frac{V_m^i \mathbf{E}_m}{1 + j\lambda_m} \right)^* d\Omega \\ &= \frac{1}{\eta} \iint_{S_\infty} \sum_{n=1}^{\infty} \frac{V_n^i \mathbf{E}_n}{1 + j\lambda_n} \cdot \sum_{m=1}^{\infty} \frac{V_m^i \mathbf{E}_m^*}{1 - j\lambda_m} d\Omega \\ &= \frac{1}{\eta} \sum_{n=1}^{\infty} \frac{(V_1 I_n(p) l_p)^2}{1 + {\lambda_n}^2} \iint_{S_\infty} \mathbf{E}_n \cdot \mathbf{E}_n^* d\Omega \\ &= \sum_{n=1}^{\infty} \frac{(V_1 I_n(p) l_p)^2}{1 + \lambda_n^2} \\ &\approx \sum_{n=1}^{N} \frac{(V_1 I_n(p) l_p)^2}{1 + \lambda_n^2} = \sum_{n=1}^{N} |\alpha_n|^2 \end{aligned} \tag{9}$$

where η is the space wave impedance and α_n is the modal weight coefficient for the n_{th} mode with a specific excitation.

When the similar approach is applied on a 2×2 antenna array system to measure its mutual coupling, the envelope correlation coefficient (ECC) is derived with (2), (6), and (7)

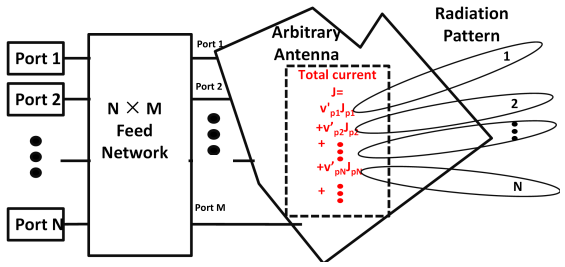

Fig. 1. Schematic view of multiport antenna radiation.

inserted

$$\rho_{ECC} = \frac{\oiint_S E_1 \cdot E_2^* d\Omega}{\sqrt{\oiint_S E_1 \cdot E_1^* d\Omega \oiint_S E_2 \cdot E_2^* d\Omega}}$$
$$= \frac{1}{\eta\sqrt{P_{rad1}P_{rad2}}} \oiint_{S_\infty} \sum_{n=1}^{\infty} \frac{V_n^{1i}\mathbf{E}_n}{1+j\lambda_n} \left(\sum_{m=1}^{\infty} \frac{V_m^{2i}\mathbf{E}_m}{1+j\lambda_m} \right)^* d\Omega$$
$$= \frac{\sum_{n=1}^{\infty}(V_1 V_2 I_n(p) I_n(q) l_p l_q)}{(1+\lambda_n^2)\sqrt{P_{rad1}P_{rad2}}}$$
$$= \sum_{n=1}^{\infty} \left(\frac{1}{\sqrt{1+\lambda_n^2}} \frac{V_1 I_n(p) l_p}{\sqrt{P_{rad1}}} \right) \left(\frac{1}{\sqrt{1+\lambda_n^2}} \frac{V_2 I_n(q) l_q}{\sqrt{P_{rad2}}} \right)$$
$$\approx \sum_{n=1}^{N} M_{1n} M_{2n} \tag{10}$$

where $((1/\sqrt{1+\lambda_n^2})(V_i I_n(p) l_p/\sqrt{P_{radi}}))$ is noted as M_{in} and will be explained later. Moreover, (9) can be normalized as

$$1 = \sum_{n=1}^{N} \frac{(V_1 I_n(p) l_p)^2}{(P_{rad1})(1+\lambda_n^2)} = \sum_{n=1}^{\infty} M_{1n}^2. \tag{11}$$

The above-mentioned derivations assume that antenna port 1 only lays on the p_{th} nonboundary mesh edge and port 2 on the q_{th} edge.

M_{1n} or M_{2n} can easily be calculated through CMA methods. Equation (11) shows the energy contribution of each mode in far-field radiation, and (10) presents how two ports are coupled at each CM in far field. Thus, we name M_{1n} as the n_{th} *modal energy occupied coefficient* (MEOC) for port 1.

III. MEOC for Multimode MIMO System

A general multimode antenna system should be constructed as shown in Fig. 1. N ports are used to feed the antenna through an $N \times M$ ($N \leq M$) feeding network and each port excites a particular radiation pattern. At low frequency, where only a few CMs have resonating potentials, high isolation is achieved once each port excites a single CM with no interference from other ports. However, the number of ports is limited as there are only a few dominant CMs at low frequency. As the frequency rises, the increased number of CMs makes it possible to realize more input ports. Nevertheless, the case becomes complex, as each port is likely to excite multiple CMs with different characterizes at the same time. Although the requirement seems to be strict, TCM can still be used to analyze the resonance and coupling from aspects of CMs.

In [13], the modal self-admittance (MSA) and modal mutual-admittance (MMA) are obtained as

$$Y_{11} = \sum_{n=1}^{\infty} MSA = \sum_{n=1}^{\infty} \frac{(I_n(p) l_p)^2}{1+j\lambda_n}$$
$$Y_{21} = \sum_{n=1}^{\infty} MMA = \sum_{n=1}^{\infty} \frac{I_n(p) I_n(q) l_p l_q}{1+j\lambda_n}. \tag{12}$$

MAs are related to the MEOC as follows:

$$M_{1n}^2 = \frac{V_1^2}{2P_{rad1}}(MSA + MSA^*)$$
$$M_{1n} M_{2n} = \frac{V_1 V_2}{2\sqrt{(P_{rad1}P_{rad2})}}(MMA + MMA^*). \tag{13}$$

Thus, the coupling matrix related to admittance matrix is

$$\mathbf{real} \begin{bmatrix} Y_{11} & \cdots & Y_{1N} \\ Y_{21} & \cdots & Y_{2N} \\ \vdots & \cdots & \vdots \\ Y_{N1} & \cdots & Y_{NN} \end{bmatrix}$$
$$= \mathbf{p} I_{N\times N} \begin{bmatrix} \sum M_{1n}M_{1n} & \cdots & \sum M_{1n}M_{Nn} \\ \sum M_{2n}M_{1n} & \cdots & \sum M_{2n}M_{Nn} \\ \vdots & \cdots & \vdots \\ \sum M_{Nn}M_{1n} & \cdots & \sum M_{Nn}M_{Nn} \end{bmatrix} (\mathbf{p} I_{N\times N})^H$$
$$= \sum_{n=1}^{\infty} \left(\mathbf{p} I_{N\times N} \begin{bmatrix} M_{1n}M_{1n} & \cdots & M_{1n}M_{Nn} \\ M_{2n}M_{1n} & \cdots & M_{2n}M_{Nn} \\ \vdots & \cdots & \vdots \\ M_{Nn}M_{1n} & \cdots & M_{Nn}M_{Nn} \end{bmatrix} (\mathbf{p} I_{N\times N})^H \right)$$
$$= \sum_{n=1}^{\infty} (\mathbf{p} I_{N\times N} [\widetilde{M_{N\times N}}] (\mathbf{p} I_{N\times N})^H) \tag{14}$$

where $\mathbf{p} = [(\sqrt{P_{rad1}}/V_1), (\sqrt{P_{rad2}}/V_2), \ldots, (\sqrt{P_{radN}}/V_N)]$ is the vector to normalize MEOC according to radiation energy from each port. $I_{N\times N}$ is a $N \times N$ unit matrix. $[\widetilde{M_{N\times N}}]$ is the matrix assignment of MEOC. N represents the number of MIMO dimension.

Equation (14) enables the utilization of typical linear matrix transformation for MEOC, and it is easy to get the following transformation:

if

$$[Y_{new}] = T[Y_0]T^H$$

then

$$[\widetilde{M_{N\times N,new}}] = \{[\mathbf{p}_{new} I]^{-1} T[\mathbf{p} I]\} [\widetilde{M_{N\times N,0}}] \{[\mathbf{p}_{new} I]^{-1} T[\mathbf{p} I]\}^H \tag{15}$$

in which $[T]$ is a $M \times N$ transformation matrix representing effects from the feeding structure, and $[Y_{new}]$, $[\widetilde{M_{N\times N,new}}]$ are the results after transformation. Diagonal elements of $[\widetilde{M_{N\times N,new}}]$ describe the energy occupancy of external ports according to CMs, while nondiagonal element describes how each port couples together in far field.

Since the normalization vector $\mathbf{p}$ varies with the input voltage amplitude, $\mathbf{p}$ is not easy to obtain in the calculation of (14)

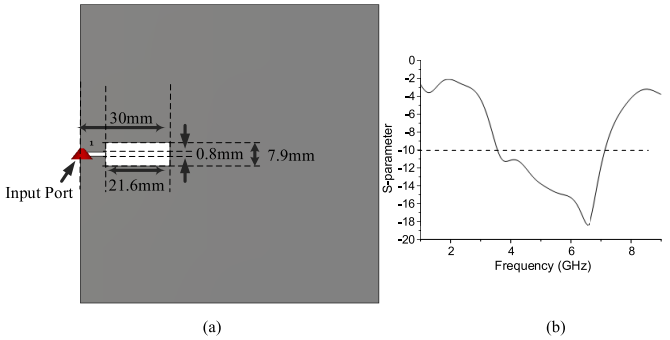

Fig. 2. Stepped slot structure. (a) Structure of the slot. (b) S-parameter of this slot. The length of the slot is 30 mm. This slot is fed at its end and works at 3–6.5 GHz.

and (15). However, we noticed that (11) makes every diagonal elements of the sum $\sum[\widetilde{M_{N\times N}}]$ to be unity, which helps to normalize each M_{in} to its right value without calculating $\mathbf{p}$.

Equations (13)–(15) tell the close relationship between MA and MEOC, though they are motivated and derived from different terms. It is noticed that MEOC is the normalized real part of MA, with the imaginary part of MA omitted. Despite the omission, the proposed MEOC is sufficient for the far-field coupling research. The derivation of MEOC in Section VI indicates that the coupling energy on the far field is linear and it can be decomposed into MEOC (or the real part of MA) for coupling comparison. The imaginary part of MA, which implies the reactance behavior of the near field, however, is nonlinear and too complex to compare. Thus, by retaining the real part and omitting the imaginary part of MA, MEOC focuses on the far-field diversity among ports and avoids considering the reactance coupling in the near field.

In Section IV, we will show MEOC's obvious advantages on the coupling analysis on multiport antennas, especially those with port number more than 2. Compared with the previous MA method, MEOC proposes a faster and clearer way to analyze couplings.

IV. Application Example With MEOC

A. Wideband Open-End Slot

An open-end slot [19], [20] is first introduced here to enable later analyses and design. As shown in Fig. 2, this stepped slot is fed at the edge and it works at 3–6 GHz. The total length of the slot is 30 mm, and the first step is 21.6 mm. Its wideband performance benefits from the stepped slot width. Since the input voltage incidents at the end of the slot, the slot has a high-input impedance (around 100 Ω). Therefore, a tapered balun structure is used to offer a balanced feed and impedance transformation at the end of design.

B. MEOC Analysis for a Rectangular Plate

The ends of four open-end slots are inserted on every outline edge of a rectangular plate, with a length of 78 mm (about $1.1\lambda_{4.5\,\mathrm{GHz}}$), and are fed through a feeding network as illustrated in Fig. 3(a). To realize MIMO operation on the suggested structure, two sets of odd and even modes are fed

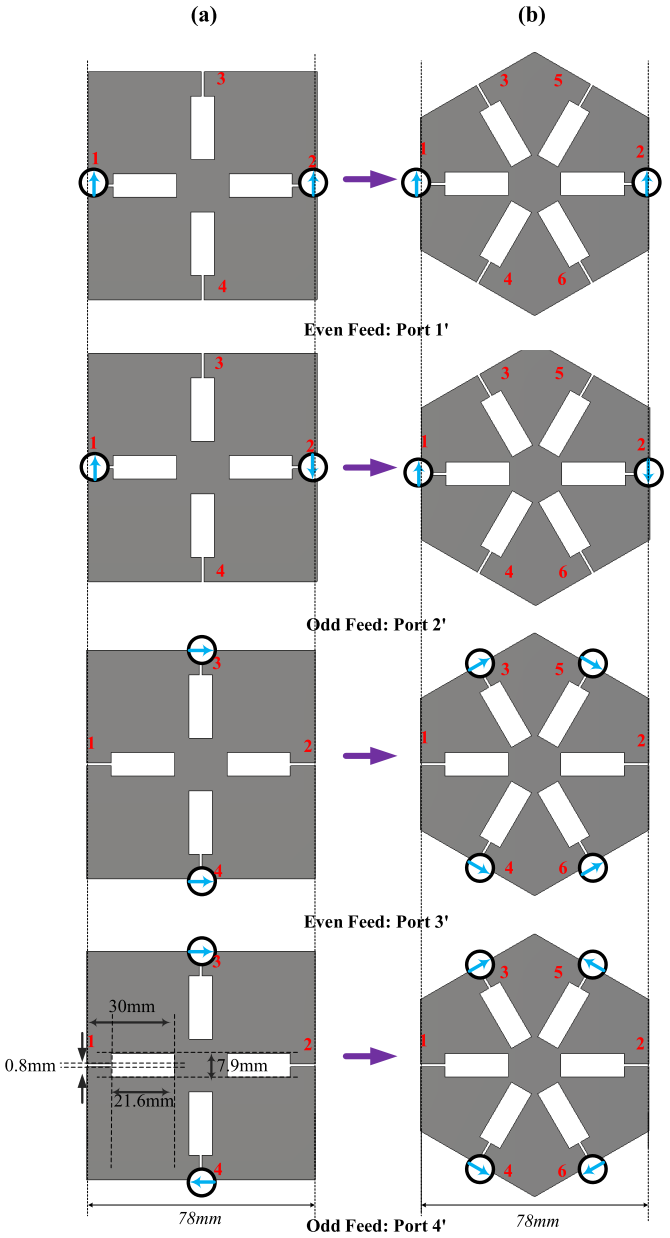

Fig. 3. Four feed schemes through four different ports 1'–4' for (a) rectangular plate and (b) hexagonal plate. The antenna ports are located at the end of each slot, which are named as ports 1–4 (rectangle) or ports 1–6 (hexagon).

based on the four feeding schemes as shown in Fig. 3(a), which can easily be realized with two 180° hybrids. The combination of input ports 1 and 2 and a 180° hybrid are usually used as the simplest decoupling feeding network on the symmetric-located antenna ports 1 and 2 [21], and the combination is applied in the same way at ports 3 and 4. For antenna ports 1 and 2, their symmetric input admittance matrix $[Y]$ can be diagonalized by decoupling matrix V_2, i.e., [22]

$$\begin{bmatrix} Y'_{11} & Y'_{12} \\ Y'_{21} & Y'_{22} \end{bmatrix} = V_2 \begin{bmatrix} Y_{11}+Y_{12} & \\ & Y_{22}-Y_{21} \end{bmatrix} (V_2)^H$$
$$V_2 = \frac{1}{\sqrt{2}} \begin{bmatrix} 1 & 1 \\ 1 & -1 \end{bmatrix} \tag{16}$$

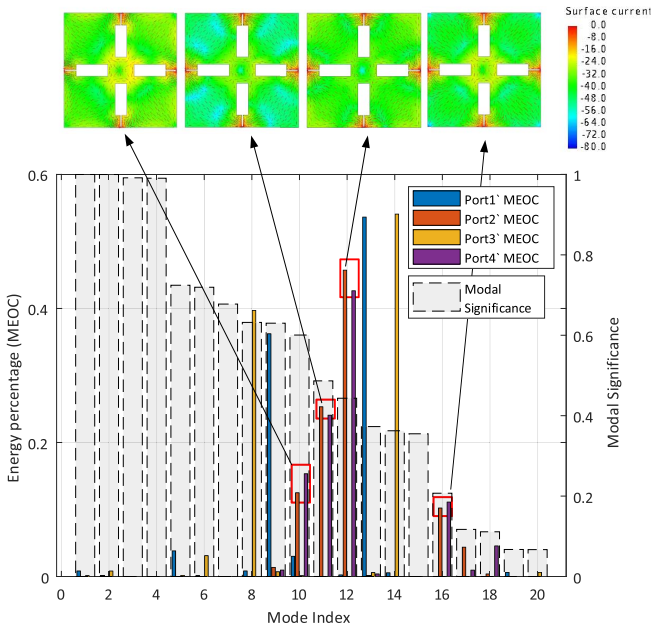

Fig. 4. MEOC analysis and MSs of rectangular plate at 4.5 GHz. It is shown that radiation by port $1'$ is dominated by Mode 4, 9, and 13. For port $2'$, the dominant modes are Modes 9–12, 16, and 17. For port $3'$, they are 6, 8, and 14. Finally, for port $4'$, they are 10–12, 16, and 18. The surface current for the shared dominant modes of ports 2 and 4 are also illustrated.

where $[Y']$ is the admittance matrix on the input ports $1'$ and $2'$ after decoupling. With the benefit of (14), the relationship between input ports 1'–4' to antenna ports 1–4 should be

$$[Y'] = T[Y]T^H$$
$$[\widetilde{M'}] = \{[\mathbf{p}'I]^{-1}T[\mathbf{p}I]\}[\widetilde{M}]\{[\mathbf{p}'I]^{-1}T[\mathbf{p}I]\}^H$$

where

$$T = \begin{bmatrix} I_{2\times 2} & \\ & V_2 \end{bmatrix}\begin{bmatrix} V_2 & \\ & I_{2\times 2} \end{bmatrix}$$
$$V_2 = \frac{1}{\sqrt{2}}\begin{bmatrix} 1 & 1 \\ 1 & -1 \end{bmatrix}. \tag{17}$$

With the help of (17), MEOC analyses at 4.5 GHz are shown in Fig. 4. We can see clearly that input ports $1'$ and $3'$ independently excite different modes and have few common modes with other ports. Hence, high isolation between the two ports and others is predicted, which can be verified by scattering parameters presented in Fig. 5(a) (solid lines). Fig. 4 also indicates that when input ports $1'$ and $3'$ are fed simultaneously, they are barely coupled at any mode. This is the MEOC-based depiction for the commonly high isolation of orthogonal-polarization antennas. On the other hand, in Fig. 4, the far fields radiated by ports $2'$ and $4'$ are mainly composed of their common Mode 10, 11, and 12, which takes up to more than 90% of the total radiate energy. It indicates a high coupling between ports $2'$ and $4'$, which matches well with simulation results in Fig. 5(a) (solid lines). Moreover, on these coupling modes, ports $2'$ and $4'$ consume equal electromagnetic energy.

To separate the symmetric energy distribution of ports $2'$ and $4'$ with least influence on the performance of ports $1'$ and $3'$, the shape of the rectangular plate is modified to a hexagonal plate with the same length, which leads to the change of excitation of ports $3'$ and $4'$ with two more ports, as shown Fig. 3(b). Excitations of ports $1'$ and $2'$ stay the same.

The matrix transformation for the hexagonal plate is similar to that of the rectangular plate, and the relationship between input ports 1'–4' and antenna ports 1–6 is

$$[Y'] = T[Y]T^H$$
$$[\widetilde{M'}] = \{[\mathbf{p}'I]^{-1}T[\mathbf{p}I]\}[\widetilde{M}]\{[\mathbf{p}'I]^{-1}T[\mathbf{p}I]\}^H \tag{18}$$

where

$$T = \begin{bmatrix} I_{2\times 2} & \\ & V_2 \end{bmatrix}\begin{bmatrix} I_{2\times 2} & \\ & D_{2\times 4} \end{bmatrix}\begin{bmatrix} V_2 & \\ & I_{4\times 4} \end{bmatrix}$$
$$D_{2\times 4} = \frac{1}{\sqrt{2}}\begin{bmatrix} 1 & 1 & & \\ & & 1 & 1 \end{bmatrix}$$
$$V_2 = \frac{1}{\sqrt{2}}\begin{bmatrix} 1 & 1 \\ 1 & -1 \end{bmatrix}. \tag{19}$$

The MEOC research and MS for the modified structure at 4.5 GHz is shown in Fig. 6(a). In Fig. 6(a), each port excites individual modes after the modification, which results in low coupling over the entire operating frequency band as proved in Fig. 5(a).

Figs. 4 and 6 illustrate the simple but clear MEOC method to analyze ports coupling not only on predicting two coupled ports but also on determining those modes that are responsible for the coupling. If the four-port antenna problem in this section is analyzed by the previous MA method [13], which is not initially designed for the multiport system, there are six MMAs and four MSAs per each mode that need to be compared in the same time, while for the newly proposed method, only one MEOC for each mode is needed. In fact, for an N-port multiport antenna, there are N MMAs and $((N)/(N-1))2$ MSAs to deal with, for every mode simultaneously, while only N in total with the MEOC method. The reason why MEOC greatly simplifies the coupling analysis is that MEOC decomposes the coupled energy on each MMA to single-modal energy on related ports, with the normalization of MSA. For example, in the rectangular antenna case, the $MMA_{1,4}$ is divided into two MEOCs: M_1 and M_4. The comparison on MSA is also omitted in MEOC method as MEOC hides the port impedance and focuses on field coupling. In summary, MEOC makes the coupling analysis much more concise, and this advantage is more pronounced when dealing with multiport antennas.

Over the other hand, it is observed from Fig. 5(b) that every port except for port $3'$ is well matched over 3–6 GHz. Therefore, the next step is to tune port $3'$ to reach a better impedance matching.

C. Impedance Matching for Hexagonal Plate

It is noticed from Fig. 6(a) that the dominant modes excited by port $3'$ are Modes 3, 4, and 7. Their corresponding surface currents (decibel) and far fields are illustrated in Fig. 6(b). Degenerated modes—Modes 3 and 4—occur due to the structure symmetry and they behave in a similar manner over the

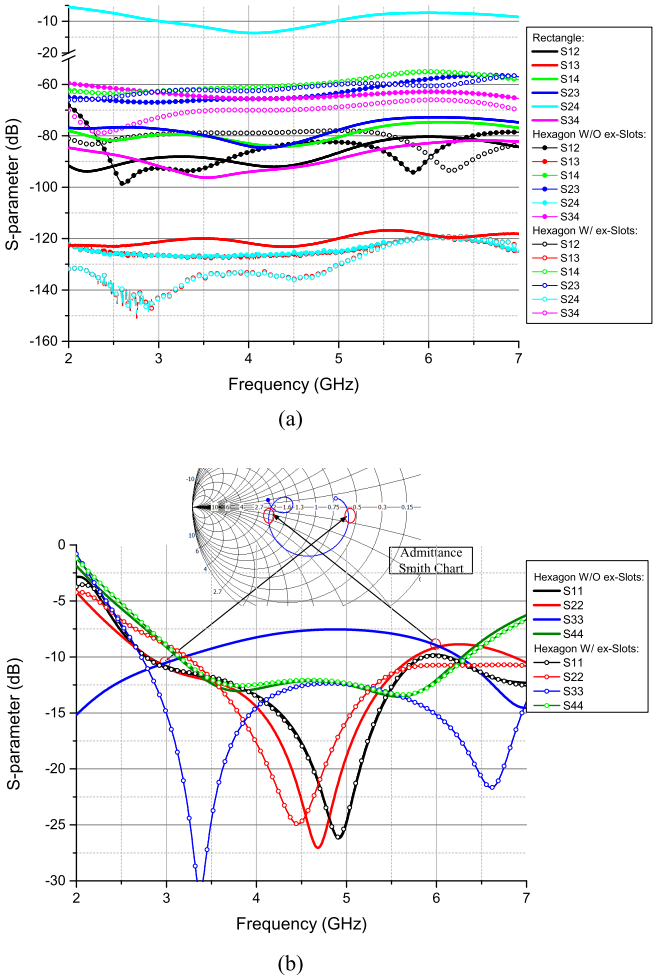

Fig. 5. Reflection and transmitting coefficients of three mentioned structure (rectangular plate, hexagonal plate, and hexagonal plate with extra slots). (a) Coupling among four ports for three structures. (b) Self-reflection coefficients for all ports on hexagonal plates.

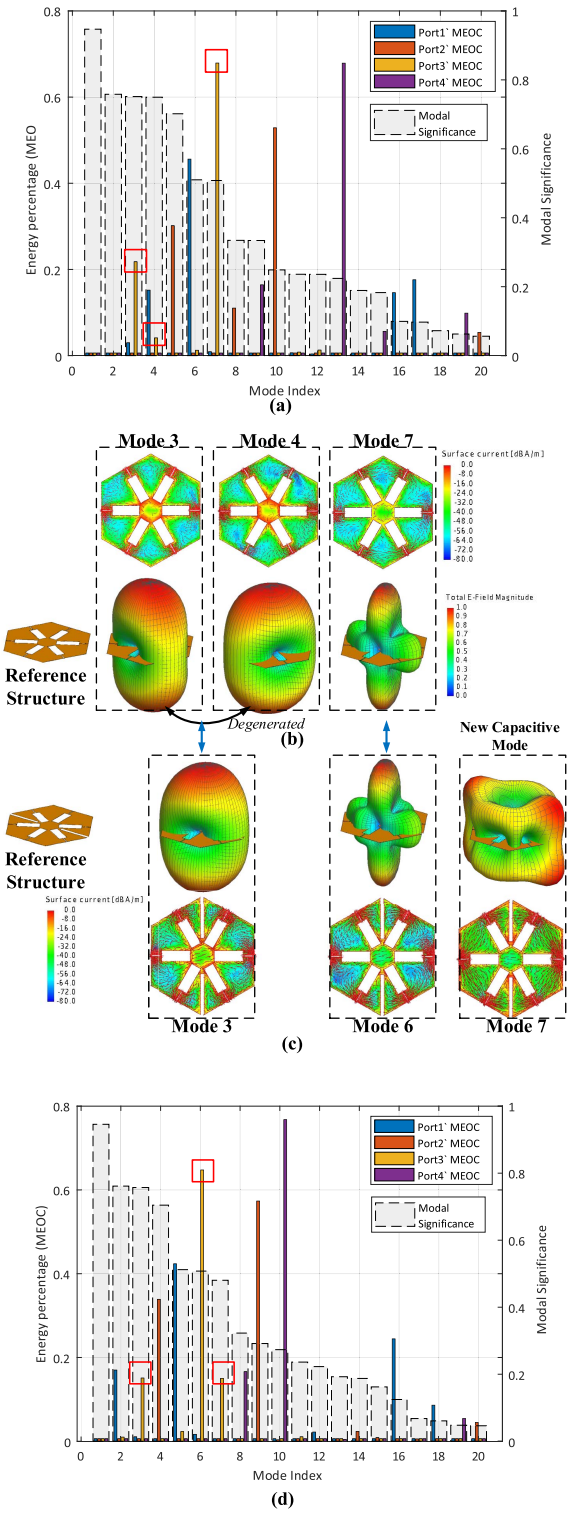

Fig. 6. MEOC research for a hexagonal plate with or without extra slots. (a) MEOC analysis and MSs for the original hexagonal plate at 4.5 GHz. (b) Three dominant modes for port 3′ of the original hexagonal plate: their current and E-field. (c) Three dominant modes for port 3 after adding extra slots. (d) MEOC analysis and MSs for the modified hexagonal plate at 4.5 GHz. The size for the extra slot is 32 mm and width 3 mm.

frequency band, which is also proved by the wideband tracking of their eigenvalues in Fig. 7 (dashed lines). In Fig. 6(b), radiations of Modes 3 and 4 are similar to that of a wide dipole at high frequency. Mode 7 radiates a pattern with main lobe and side lobes in the diagonal plane. The wideband tracking of these mode's eigenvalues in Fig 7 (dashed lines) reveals that in the operating frequency band 3–6 GHz, Modes 3 and 4 have already passed their resonant frequencies and both of them have positive eigenvalues, which, according to (3), indicates that they store magnetic energy over the operating frequency band. In addition, Mode 7 does not resonate at all over the operating frequency and it also has a positive eigenvalue. Therefore, all the dominant modes store a large amount of magnetic energy within the frequency band, which makes the impedance matching at port 3′ difficult to be implemented. This fact conforms to the inductive behavior of port 3′ illustrated in the admittance Smith chart in Fig. 5(b).

Hence, a capacitive component is added to the structure to improve the matching of port 3′. Two slots are cut along the long diagonal of the hexagonal plate, as shown in Fig. 6(c). These slots introduce a new capacitive Mode 7 dominating port 3′, which has far field main lobes symmetric in the diagonal plane, as illustrated in Fig. 6(c) and (d). Besides, after modification, there is no degenerated modes dominating

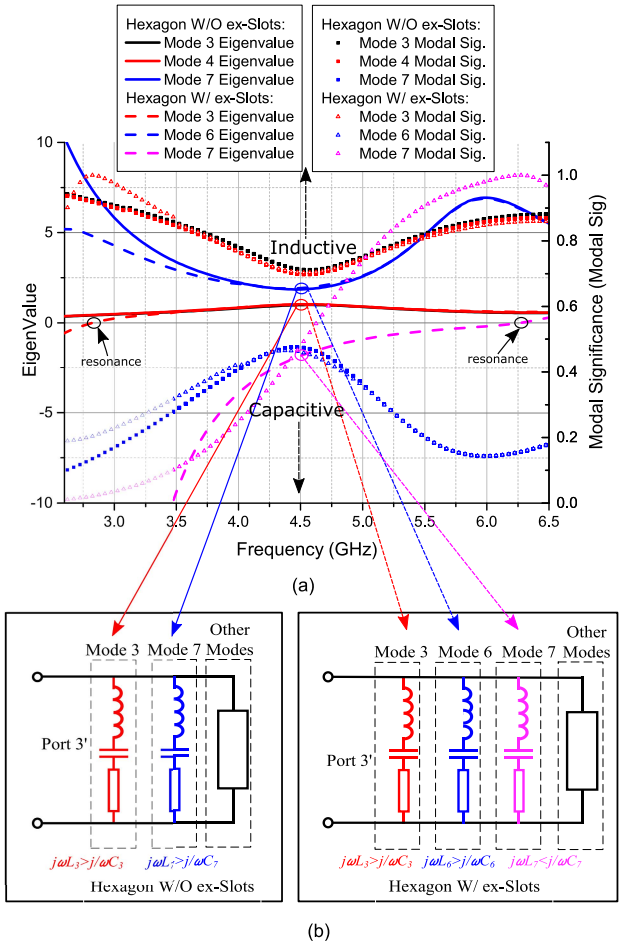

Fig. 7. Comparison of dominant modes between two hexagonal plates with or without extra slots. (a) Eigenvalue and MS of port 3′'s dominant modes at 2.6–6.5 GHz of two hexagonal plates. (b) Equivalent circuit for two hexagonal plates with reference to port 3′.

port 3′ but only Mode 3 radiating a "dipolelike" pattern. This is because the new slots restrict the number of hexagon's symmetry axis at diagonal to only 1, which makes only one mode in the degenerated pair reactive with reference to port 3′. Moreover, the original Mode 7 now shifts to Mode 6, and its far-field pattern barely changes at 4.5 GHz, as the new slots are located at the current weak area of the original Mode 7.

Eigenvalues for new dominant modes and their corresponding MS are shown in Fig. 7(a) (solid lines with bubbles). From the results, the new Mode 7 resonates at 6.3 GHz and behaves inductively at 3–6 GHz. Eigenvalues of new Modes 3 and 6 barely change compared to those of the originally structure and have positive values in the operating band. Mode 3 is a "dipolelike" mode, and adding slots is equivalent to shorten the electrical length of the wide dipole. Therefore, its resonance frequency raises to 2.8 GHz.

Modes 3 and 4 of the original hexagon and Mode 3 of the modified one have passed their resonant frequencies and behave inductively with positive eigenvalues. In a schematic view, Modes 3 and 4 can be equivalent to a first-order series RLC subcircuit where $j\omega L > j/(\omega C)$ over the frequency band. Mode 7 of the original hexagon and Mode 6 of the modified one do not resonate in the band and have high positive eigenvalues. Therefore, they are also equivalent to a subcircuit in which $j\omega L > j/(\omega C)$. As for the new Mode 7 after adding slots, which resonates at 6.3 GHz and has negative eigenvalues over the frequency band, it is equivalent to a subcircuit whose $j\omega L < j/(\omega C)$.

Equivalent circuits discussed earlier are then assigned into a paralleled circuit as shown in Fig. 7(b) with their corresponding parameters at 4.5 GHz listed in Table I. Values of the circuit components are obtained from

$$R_n\sqrt{\frac{L_n}{C}} = Q = \frac{\omega}{2}\sqrt{\left(\frac{2I'_{port}}{I_{port}}\right)^2 + \left(\lambda'_n - 2\frac{\lambda_n I'_{port}}{I_{port}} + \frac{|\lambda_n|}{\omega}\right)^2}, \quad [23]$$

$$R_n + j\omega L_n - j\frac{1}{\omega C_n} = MSA_n = \frac{I^2_{port}}{1 + j\lambda_n} \quad (20)$$

where R, L, and C are the equivalent circuit components. Q is the quality factor. I'_{port} and λ'_n are derivatives of port current and eigenvalue at 4.5 GHz. Resistors in each subcircuit represent the modes dominate the radiation. For other modes that do not have much contribution to the radiation, their equivalent resistances are large enough to be omitted in the parallel circuit. Thus, their reactance can be over all equivalent to a pure reactance. As the equivalent circuit is not the main concern of this paper, other details for the calculation will not be discussed further.

Before adding slots on the hexagon, the imaginary part of the input admittance at port 3′ is too large to be matched because of the inductive behavior of Modes 3, 4, and 7. After cutting slots, Mode 7 appears and acts as a strong capacitive mode in the band to compensate the imaginary part of the input admittance and to help match the impedance. The new capacitive Mode 7 (resonating at 6.3 GHz itself) and the original Mode 3 (resonating at 2.85 GHz itself) in parallel create two resonates (3.4 and 6.6 GHz), as shown in Fig. 5(b) (blue lines).

Fig. 7 indicates that with the increase of frequency, although a mode has already passed its resonance, or it has yet to resonant, it still has much chance to radiate, e.g., the Modes 3 and 7 of the structure with extra slots. Actually, the eigenvalue of one mode could fluctuate within a low-value range before or after the mode passing its resonate frequency, and it still makes this mode possible to participate much in radiation. In addition, if one mode does not resonate at all in the frequency band, it does not mean the mode has no contribution to the radiation. Take the Mode 6 (Fig. 7, blue line) of the hexagonal plate with an extra slot as an example. Its MS is always lower than 0.5 in the whole band, and it does not resonate at all in or out of the band, yet it still plays as an important role in the radiation. In general, eigenvalue alone does not determine the radiation ability of one mode with respect to the port. MEOC, on the other hand, describes not only how much a mode participates

TABLE I

PARAMETERS FOR THE TWO EQUIVALENT CIRCUITS IN FIG. 7(b) AT 4.5 GHz

Parameter (W/O ex-Slots)	R_3	ωL_3	$1/(\omega C_3)$	R_7	ωL_7	$1/(\omega C_3)$			
Value (Ω)	448.6	4359.4	3965.7	65.8	537.4	425.9			
Parameter (W/ ex-Slots)	R_3	ωL_3	$1/(\omega C_3)$	R_6	ωL_6	$1/(\omega C_6)$	R_7	ωL_7	$1/(\omega C_7)$
Value (Ω)	527.6	8901.0	8445.8	55.3	576.2	482.4	213.6	693.9	1083.8

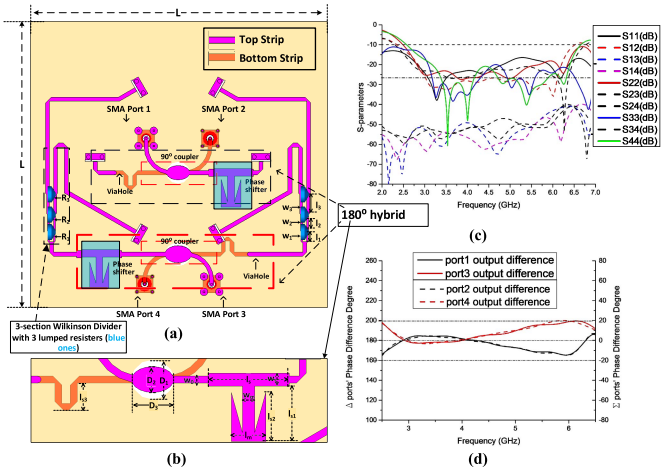

Fig. 8. Feeding network with its performance. (a) Top view of feeding network. (b) Detail of the 180° hybrid. (c) Simulation performance of the feeding network. (d) Phase responses of the feeding network. The feeding network has four input ports with an SMA connector. Its ends connect to six balun structures which are vertical to the ground. The corresponding parameters are listed in Table II.

in the radiation but also how the mode contributes to the mutual coupling.

V. ANTENNA REALIZATION AND MEASUREMENT

A. Feeding Network Design

In order to feed the hexagonal antenna, a feeding network is required to fulfill the desired feeding scheme. The feeding network needs to be planar, low lossy, and easy to combine with balun structures. As a result, a set of five-layer feeding network is designed as shown in Fig. 8(a) and (b) with corresponding parameters listed in Table II. This feeding network serves as a 4×6 transformation matrix between feeding ports and hexagon ports. The design is based on a *Rogers RO*4003 PCB board with a relative permittivity of 3.38 and a thickness of 0.813 mm.

Ports 1 and 2 are the sum (Σ) and difference (Δ) ports in a 180° hybrid, respectively. This 180° hybrid origins from the coupler in [24], which consists of three conductor layers with two layers of dielectrics. Two input ports are on different sides of the ground, and the bottom and top mircrostrips couple with each other via an elliptical-shaped slot in the ground. This microstrip-slot-microstrip transition leads to an ultrawideband (UWB) transmission characteristic. To compensate another 90° difference, the UWB phase shift in [25] is utilized to complete the 180° hybrid and maintain a constant phase shift over a wide frequency band. Making use of a T-shaped open end stub load, the phase shifter exhibits

TABLE II

PARAMETERS FOR FEEDING NETWORK IN FIG. 8

Parameter	l_1	l_2	l_3	w_1	w_2	w_3	w_0
Value (mm)	5.2	8.2	9.4	0.7	0.93	1.4	1.8
Parameter	D_1	D_2	D_3	w_s	l_s	l_{s1}	l_{s2}
Value (mm)	5.1	3.32	5.4	3.3	21	14.2	12.9
Parameter	l_{s3}	l_m	w_m	L	R_1	R_2	R_3
Value (mm)	7	8.9	3.18	150	98	123.9	341

a better bandwidth than conventional 90° phase shifter. The detailed theoretical analyses for the 180° hybrid are skipped here for the sake of concision. The reflection performance and transmitting phase difference of the feeding network can be shown in Fig. 8(c) and (d). It is verified in Fig. 8(d) that phase differences for all ports are stabilized at $0° \pm 20°$ (for Σ ports) or $180° \pm 20°$ (for Δ ports) at 2.5–6.5 GHz. A similar hybrid has also been constructed for ports 3 and 4, except for a pair of three-section Wilkison dividers cascading at each end of the 180° hybrid to feed antenna ports equally and maintain isolation. It should be noticed that the original hybrid in [24] has its input and output ports on different sides of the ground plane. In this paper, in order to attach and fix, the balun structure on the top of the feeding network, two vias are used to make sure the end strip of the whole feeding network is on the topside of the ground.

B. Final Combination

The final combination of the whole structure is shown in Fig. 9. From bottom to top, there are three main components, a five-layer feeding network board, six tapered balun structures in the vertical position, and the antenna board. The feeding network is fed through four SMA connectors on the bottom side of the feeding network board. This board is a five-layer structure, with microstrip traces on both sides (Layers 1 and 2) and ground (Layer 3) in the center layer. Details of the feeding network can be found in Section VI. Six balun structures, behaving as smooth impedance converters and providing balanced feeds to the antenna, connect the feeding network and the antenna board. For the antenna board, the metallic part is on its bottom side and the dielectric is on the top.

Both the balun structure and the feeding network utilize *Rogers RO*4003 PCB board with a relative permittivity of 3.38 and a thickness of 0.813 mm. The antenna board uses *Rogers RT*5870 Laminates with a relative permittivity of 2.33 and a thickness of 0.508 mm.

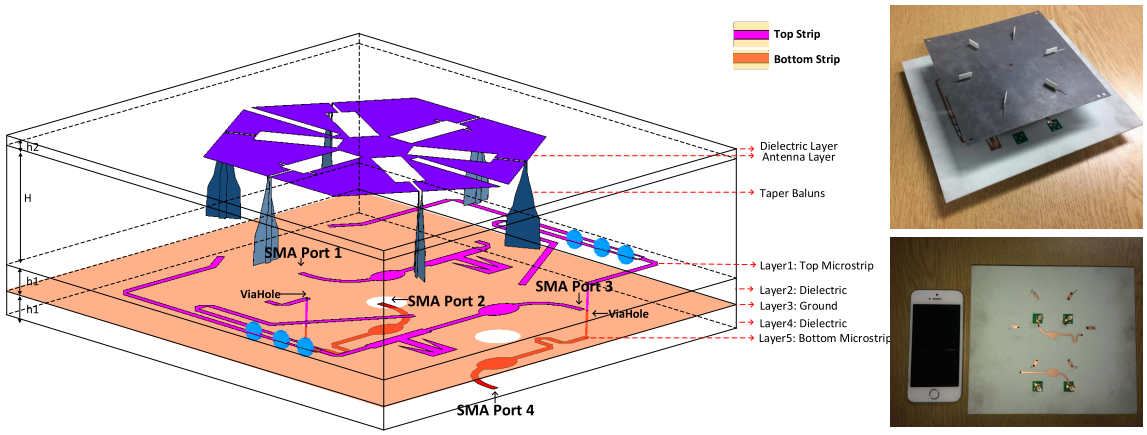

Fig. 9. Final combination of antenna, balun, and feeding network. (a) Exploded view of the design. (b) Perspective view and back view. The antenna is fed through four SMA connectors on the bottom side of the ground. $h1 = 0.813$ mm, $h2 = 0.518$ mm, and $H = 23$ mm.

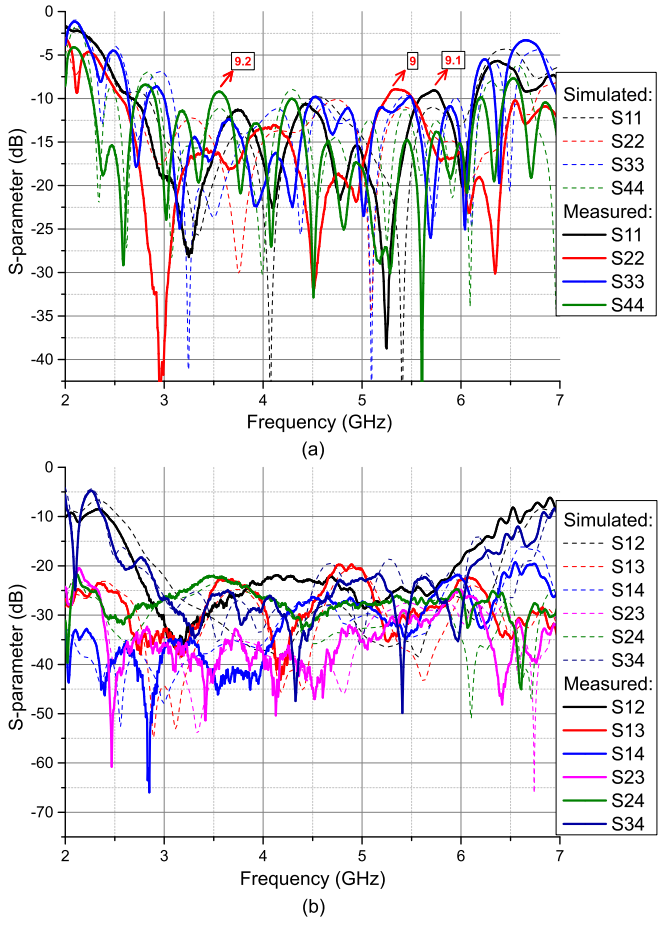

Fig. 10. Scattering parameters of the antenna. It works well at 3–6 GHz, with isolation lower than −20 dB. (a) Port reflection. (b) Isolation among ports.

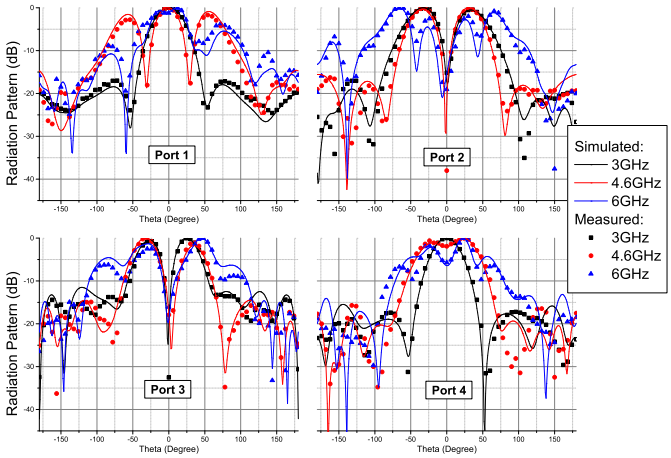

Fig. 11. Far-field pattern of all four ports at three frequencies (3, 4.6, and 6 GHz) at yz plane.

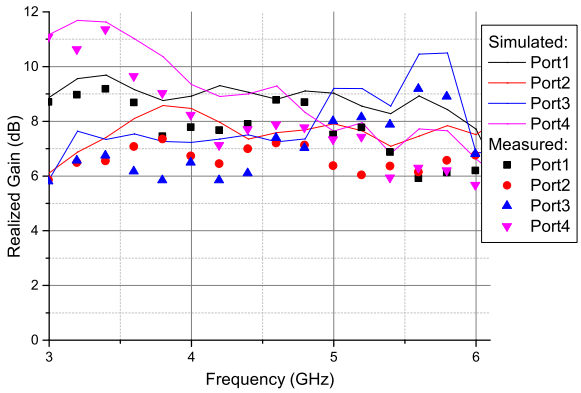

Fig. 12. Realized gain of all ports at 3–6 GHz.

C. Simulated and Measured Results

As described in Section VI, all parts of the proposed antenna are fabricated and combined, as shown in Fig. 9. The prototype is then measured with a four-port network analyzer in an anechoic chamber. The corresponding scattering parameters are illustrated in Fig. 10. As shown in Fig. 10, reflection coefficients of all channels are below −10 dB across 3–6 GHz, except for a few discrete frequencies having a maximum value of −9 dB in measurement. The proposed

structure achieves a fractional impedance bandwidth of 66.7%, and both the simulated and measured port-to-port isolations are lower than −20 dB over the entire frequency band. The measurement results match well with simulations, though there are slight frequency shifts on some ports, which is likely to be caused by the soldering errors of the SMA connectors. In Figs. 11 and 12, the simulated and measured radiation patterns and realized gains of all ports are compared. Effects of cables and unavoidable scattering in the chamber could be the source of minor discrepancies between measurement and simulation results, and gains of all ports are higher than 6 dBi.

VI. Conclusion

In this paper, a new method, the evaluation of multimode antenna's modal coupling and radiation, is introduced. Further derivation has been presented to enable the method to be adopted in the linear transformation of a feeding network. This method shows its advantages by decomposing the mutual energy occupancy state of each mode to give a clear view for the radiation and mutual coupling of an MIMO antenna. The MEOC can also be used to evaluate the dominant modes and to further improve the impedance matching. Based on this, a hexagonal wideband antenna is proposed as an example. The proposed antenna uses multiport on a single radiator, which provides broadband (a relative bandwidth of 66.7%) performance for four ports within a compact structure. It is also shown that the isolation of this antenna is high enough over its working frequency band.

References

[1] T. Svantesson, "An antenna solution for MIMO channels: The multimode antenna," in *Proc. Conf. Rec. 34th Asilomar Conf. Signals, Syst. Comput.*, vol. 2, Nov. 2000, pp. 1617–1621.

[2] N. Herscovici, C. Christodoulou, E. Rajo-Iglesias, O. Quevedo-Teruel, and M. Sanchez-Fernandez, "Compact multimode patch antennas for MIMO applications [wireless corner]," *IEEE Antennas Propag. Mag.*, vol. 50, no. 2, pp. 197–205, Apr. 2008.

[3] J. Sarrazin, Y. Mahe, S. Avrillon, and S. Toutain, "A new multimode antenna for MIMO systems using a mode frequency convergence concept," *IEEE Trans. Antennas Propag.*, vol. 59, no. 12, pp. 4481–4489, Dec. 2011.

[4] T. Q. Tran and S. K. Sharma, "Radiation characteristics of a multimode concentric circular microstrip patch antenna by controlling amplitude and phase of modes," *IEEE Trans. Antennas Propag.*, vol. 60, no. 3, pp. 1601–1605, Mar. 2012.

[5] Z. Zhang, S. Xiao, Y. Li, and B.-Z. Wang, "A circularly polarized multimode patch antenna for the generation of multiple orbital angular momentum modes," *IEEE Antennas Wireless Propag. Lett.*, vol. 16, pp. 521–524, Jul. 2017.

[6] D. Manteuffel and R. Martens, "Compact multimode multielement antenna for indoor UWB massive MIMO," *IEEE Trans. Antennas Propag.*, vol. 64, no. 7, pp. 2689–2697, Jul. 2016.

[7] A. Araghi and G. Dadashzadeh, "Oriented design of an antenna for MIMO applications using theory of characteristic modes," *IEEE Antennas Wireless Propag. Lett.*, vol. 11, pp. 1040–1043, Aug. 2012.

[8] E. Antonino-Daviu, M. Cabedo-Fabres, M. Gallo, M. Ferrando-Bataller, and M. Bozzetti, "Design of a multimode MIMO antenna using characteristic modes," in *Proc. 3rd Eur. Conf. Antennas Propag.*, Mar. 2009, pp. 1840–1844.

[9] D. Yang, H. Zeng, R. Chen, J. Qu, Y. Wen, and S. Liu, "Four port compact multimode patch antenna system for vehicular application," in *Proc. IEEE Int. Workshop Electromagn., Appl. Student Innov. Competition (iWEM)*, May 2016, pp. 1–3.

[10] Z. Miers and B. K. Lau, "Design of multimode multiband antennas for MIMO terminals using characteristic mode analysis," in *Proc. IEEE Antennas Propag. Soc. Int. Symp. (APSURSI)*, Jul. 2014, pp. 1429–1430.

[11] M. Bouezzeddine and W. L. Schroeder, "Design of a wideband, tunable four-port MIMO antenna system with high isolation based on the theory of characteristic modes," *IEEE Trans. Antennas Propag.*, vol. 64, no. 7, pp. 2679–2688, Jul. 2016.

[12] J. Ethier and D. A. McNamara, "Through the looking glass: A characteristic mode view of electromagnetic modeling & design," in *Proc. 14th Int. Symp. Antenna Technol. Appl. Electromagn. Am. Electromagn. Conf.*, Jul. 2010, pp. 1–4.

[13] Q. Wu, W. Su, Z. Li, and D. Su, "Reduction in out-of-band antenna coupling using characteristic mode analysis," *IEEE Trans. Antennas Propag.*, vol. 64, no. 7, pp. 2732–2742, Jul. 2016.

[14] R. Garbacz and R. Turpin, "A generalized expansion for radiated and scattered fields," *IEEE Trans. Antennas Propag.*, vol. AP-19, no. 3, pp. 348–358, May 1971.

[15] R. Harrington and J. Mautz, "Theory of characteristic modes for conducting bodies," *IEEE Trans. Antennas Propag.*, vol. AP-19, no. 5, pp. 622–628, Sep. 1971.

[16] R. Harrington, J. Mautz, and Y. Chang, "Characteristic modes for dielectric and magnetic bodies," *IEEE Trans. Antennas Propag.*, vol. AP-20, no. 2, pp. 194–198, Mar. 1972.

[17] Y. Chen and C. Wang, *Characteristic Modes: Theory and Applications in Antenna Engineering*. Hoboken, NJ, USA: Wiley, 2015.

[18] S. Makarov, *Antenna and EM Modeling With MATLAB*. Hoboken, NJ, USA: Wiley, 2002.

[19] R. Kumar, R. K. Khokle, and R. V. S. R. Krishna, "A horizontally polarized rectangular stepped slot antenna for ultra wide bandwidth with boresight radiation patterns," *IEEE Trans. Antennas Propag.*, vol. 62, no. 7, pp. 3501–3510, Jul. 2014.

[20] W. Zhu, T.-P. Yu, and W.-M. Ni, "Design of a high-gain wideband microstrip antenna with a stepped slot structure," in *Proc. Int. Symp. Antennas Propag.*, vol. 1, Oct. 2013, pp. 115–117.

[21] B. Yang and J. J. Adams, "Systematic shape optimization of symmetric MIMO antennas using characteristic modes," *IEEE Trans. Antennas Propag.*, vol. 64, no. 7, pp. 2668–2678, Jul. 2016.

[22] S. K. Chaudhury, H. J. Chaloupka, and A. Ziroff, "Multiport antenna systems for MIMO and diversity," in *Proc. 4th Eur. Conf. Antennas Propag.*, Apr. 2010, pp. 1–5.

[23] J. L. T. Ethier and D. A. McNamara, "Antenna shape synthesis without prior specification of the feedpoint locations," *IEEE Trans. Antennas Propag.*, vol. 62, no. 10, pp. 4919–4934, Oct. 2014.

[24] A. M. Abbosh and M. E. Bialkowski, "Design of compact directional couplers for UWB applications," *IEEE Trans. Microw. Theory Techn.*, vol. 55, no. 2, pp. 189–194, Feb. 2007.

[25] S. Y. Zheng, W. S. Chan, and K. F. Man, "Broadband phase shifter using loaded transmission line," *IEEE Microw. Wireless Compon. Lett.*, vol. 20, no. 9, pp. 498–500, Sep. 2010.

Wei Su received the B.S. and M.S. degrees in electrical engineering from Beihang University, Beijing, China, in 2011 and 2016, respectively. He is currently pursuing the Ph.D. degree with the Whitespace Machine Communication Lab and the Antennas and Electromagnetics Group, School of Electronic Engineering and Computer Science, Queen Mary University of London, London, U.K.

His current research interests include the theory of characteristic modes and the analysis of mutual coupling among antenna elements.

Qianyun Zhang (S'14–M'18) received the B.Sc. degree (First Class Hons.) in telecommunications engineering from the Beijing University of Posts and Telecommunications, Beijing, China, in 2014, and the Ph.D. degree in electronic engineering from the Queen Mary University of London, London, U.K., in 2018.

She is currently a lecturer with the School of Cyber Science and Technology, Beihang University, Beijing, China. Her research interests include characteristic mode analysis, 5G base station antennas, compact UHF and UWB antennas, and their applications on TV white space and M2M/Internet of Things.

Shaker Alkaraki (S'17) received the B.Sc. degree (Hons.) in communication engineering from International Islamic University Malaysia, Kuala Lumpur, Malaysia, in 2011, and the M.Sc. degree (Hons.) from the University of Manchester, Manchester, U.K., in 2013. He is currently pursuing the Ph.D. degree with the Whitespace Machine Communication Lab and the Antennas and Electromagnetics Group, School of Electronic Engineering and Computer Science, Queen Mary University of London, London, U.K.

His current research interest includes 3-D printed antennas, metalizations techniques, 5G antennas and systems, high-gain corrugated plate antennas, MIMO and massive MIMO, leaky waves, and millimeter-wave antennas.

Dr. Alkaraki was a recipient of the IIUM Scholarship, UoM MSc Scholarship, and QMUL Ph.D. Scholarship.

Yao Zhang was born in Jingmen, Hubei, China. He received the B.S. degree in electronics and information engineering from the Xi'an University of Science and Technology, Xi'an, China, in 2013. He is currently pursuing the Ph.D. degree with the School of Electronic and Information Engineering, South China University of Technology, Guangzhou, China.

In 2014, he was a Researcher with the City University of Hong Kong Shenzhen Research Institute, Shenzhen, China. In 2018, he joined the Department of Electrical and Computer Engineering, Duke University, Durham, NC, USA, as a Visiting Scholar under the financial support from China Scholarship Council. His current research interests include surface acoustic wave filters, bulk acoustic wave resonators, microwave circuits, massive MIMO antennas, and integration designs of filter and antenna.

Mr. Zhang was a recipient of the Best Student Paper Award at the IEEE 5th Asia-Pacific Conference on Antenna and Propagation and the National Scholarship for Graduate Students in 2015, 2016, and 2017. He serves as a reviewer for several international journals such as the IEEE TRANSACTIONS ON ANTENNAS AND PROPAGATION and *IET Electronics Letters*.

Xiu-Yin Zhang (S'07–M'10–SM'12) received the B.S. degree in communication engineering from the Chongqing University of Posts and Telecommunications, Chongqing, China, in 2001, the M.S. degree in electronic engineering from the South China University of Technology, Guangzhou, China, in 2006, and the Ph.D. degree in electronic engineering from the City University of Hong Kong, Hong Kong, in 2009.

From 2001 to 2003, he was with ZTE Corporation, Shenzhen, China. From 2006 to 2007, he was a Research Assistant with the City University of Hong Kong, where he was a Research Fellow from 2009 to 2010. He is currently a Full Professor and Vice Dean with the School of Electronic and Information Engineering, South China University of Technology. He serves as the Deputy Director of the Guangdong Provincial Engineering Research Center of Antennas and RF Techniques, China, and the Vice Director of the Engineering Research Center for Short-Distance Wireless Communications and Network, Ministry of Education, China. He has authored or co-authored more than 100 internationally referred journal papers including more than 80 IEEE journal papers and around 60 conference papers. His current research interests include microwave circuits and subsystems, antennas and arrays, wireless power transfer.

Dr. Zhang is a Fellow of the Institution of Engineering and Technology. He served as a Technical Program Committee Chair/Member and a Session Organizer/Chair for a number of conferences. He was a recipient of the National Science Foundation for Distinguished Young Scholars of China, the Young Scholar of the Changjiang Scholars Program of Chinese Ministry of Education, the Top-Notch Young Professionals of National Program of China, and the Scientific and Technological Award (First Honor) of Guangdong Province. He was a supervisor of several conference best paper award winners. He is an Associate Editor for the IEEE ACCESS.

Yue Gao (S'03–M'07–SM'13) received the Ph.D. degree from the Queen Mary University of London (QMUL), London, U.K., in 2007.

He was a Research Assistant, a Lecturer (Assistant Professor), and a Senior Lecturer (Associate Professor) with QMUL. He is currently a Reader in antennas and signal processing, and the Director of the Whitespace Machine Communication Lab, School of Electronic Engineering and Computer Science, QMUL. He is also leading a team developing theoretical research into practice in the interdisciplinary area among smart antennas, signal processing, spectrum sharing, and Internet of Things applications. He has authored or co-authored more than 150 peer-reviewed journal and conference papers and two book chapters. He holds two patents.

Dr. Gao is an Engineering and Physical Sciences Research Council Fellow from 2018 to 2023. He served as the Signal Processing for Communications Symposium Co-Chair for the IEEE ICCC 2016, the Publicity Co-Chair for the IEEE GLOBECOM 2016, the Cognitive Radio Symposium Co-Chair for the IEEE GLOBECOM 2017, and the General Chair for the IEEE WoWMoM and iWEM 2017. He is a Secretary of the IEEE Technical Committee on Cognitive Networks and the IEEE Distinguished Lecturer of the Vehicular Technology Society. He was a co-recipient of the EU Horizon Prize Award on Collaborative Spectrum Sharing in 2016, and the Research Performance Award from the Faculty of Science and Engineering at QMUL in 2017. He is an Editor for the IEEE TRANSACTIONS ON VEHICULAR TECHNOLOGY, IEEE WIRELESS COMMUNICATIONS LETTERS, and *China Communications*.